JOURNAL OF PROPULSION AND POWER
Vol. 23, No. 2, March–April 2007

Mean Flow Approximations for Solid Rocket Motors with Tapered Walls

Oliver C. Sams IV,* Joseph Majdalani,† and Tony Saad‡
University of Tennessee Space Institute, Tullahoma, Tennessee 37388

DOI: 10.2514/1.15831

Current ballistics analyses require detailed information of the internal flowfield forming in the combustion chamber of solid rocket motors. In this study, we develop a model applicable to the circular-port motor with slightly tapered grain. A combined geometric configuration is considered in which a straight cylinder is connected to a tapered cone. The analysis is based on the vorticity-stream function approach, allowing us to resolve the problem under incompressible, isothermal, inviscid, rotational, axisymmetric, and steady-state conditions. Additionally, Clayton's procedure is implemented with the aim of producing an approximate solution that reflects the behavior of the flowfield at higher orders in the taper angle (Clayton, C. D., "Flowfields in Solid Rocket Motors with Tapered Bores," AIAA Paper 96-2643, July 1996). Given a nonlinear governing equation, a solution is sought with the use of regular perturbations. A numerical simulation is also carried out, based on a finite volume solver, to verify the asymptotic approximations. Analytical results are discussed and their range of validity is determined. The pressure recovery due to taper is calculated and shown to be important in most practical applications.

Nomenclature

F	=	momentum thrust
p	=	normalized pressure, $\bar{p}/\rho V_b^2$
$\bar{p}$	=	dimensional pressure
R_0	=	dimensional radius of cylindrical motor
r	=	normalized radial coordinate, $\bar{r}/R_0$
$\bar{r}$	=	dimensional radial coordinate
$\boldsymbol{u}$	=	normalized velocity, $\bar{\boldsymbol{u}}/V_b$
$\bar{\boldsymbol{u}}$	=	dimensional velocity, $(\bar{u}_r, \bar{u}_z)$
V_b	=	injection velocity at propellant surface
z	=	normalized axial coordinate, $\bar{z}/R_0$
$\bar{z}$	=	axial coordinate
β	=	velocity ratio, $u_{\max}/u_{\text{ave}}(z)$
η	=	coordinate transformation, $\eta \equiv \beta_0 r^2/r_s^2$
ρ	=	density
ψ	=	normalized stream function
Ω	=	normalized vorticity

Subscripts

b	=	burning surface
r, z	=	radial or axial component
θ	=	azimuthal component
0	=	leading-order, parallel chamber quantities
1	=	first-order correction

Superscript

$-$	=	dimensional quantity

I. Introduction

THE extraction of critical design parameters for solid rocket motors (SRMs) through internal ballistics analysis constitutes an integral part of modern propulsion system design and development. The flowfields generated in combustion chambers and their performance comprise the framework necessary to evaluate specific motor requirements, candidate grain geometries, motor configurations, and propellant formulations [1]. Ballistics analyses are available to predict chamber pressures, combustion instabilities, thrust, mass flux, and grain burn rate histories based on the velocity and pressure profiles provided by the mean flowfield [2–9]. An increase in the accuracy of predictions provided by ballistics analyses invariably requires enhanced flowfield models.

In the past, several researchers have developed mean flow models that have set the standard for flowfield investigations. Among them is Culick [10], whose original rotational, inviscid solution remains at the foundation of many studies. These include those by Majdalani and coworkers who have extended Culick's solution by capturing the effects of viscosity, wall regression [11,12], compressibility [13], and arbitrary headwall injection [14,15]. Other related research involves the evaluation of unsteady wave motions [16–21], acoustic interactions with propellant burning [12], velocity and pressure coupling [22], nonlinear (DC) pressure shift [23], triggering amplitudes [24], limit cycle amplitudes [25], as well as particle-mean flow interactions [26–30], two-phase flow effects [31], distributed combustion, parietal vortex shedding [32–34], and both spatial and temporal instabilities of the mean flow [35–38].

It is imperative that the rocket propulsion community continues to seek refinement in current analytical, numerical, and experimental flowfield modeling methods to avoid economic losses resulting from adjusted mission requirements, overdesign, mission failures, and catastrophic accidents due to under and overprediction of the pressure load in the motor case.

The search for enhanced analytical models has led one to consider the mean flowfield characteristics of SRMs with tapered bores. Examples of tapered propellant surfaces can be observed in the Titan IV, Ariane, Castor, solid rocket boosters, interceptor vehicles with fast burning propellants, and other moderate size launch vehicles requiring thrust curve modifications. Most modern SRMs are manufactured with small tapers to facilitate the removal of the casting mandrel after the curing process is completed. It is implied that these small tapers help to reduce the contact between the propellant surface and the mandrel, thereby reducing the possibilities of propellant tear, cracking and debonding. Additional tapering of propellant bores has served two functions: 1) minimization of erosive burning and 2) implementation of boost-sustain motor configurations. Tapering or coning of the propellant surfaces can also help to

Received 23 March 2005; accepted for publication 16 June 2006.

*Graduate Research Associate. Member AIAA.
†Jack D. Whitfield Professor of High Speed Flows, Department of Mechanical, Aerospace and Biomedical Engineering. Member AIAA.
‡Doctoral Research Assistant. Member AIAA.

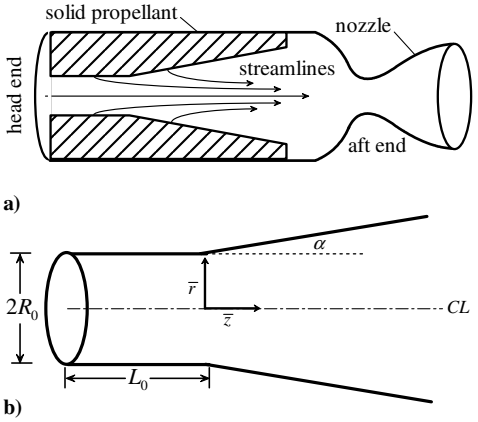

Fig. 1 Schematic featuring a) typical cylindrical solid rocket motor with tapered bore and characteristic streamlines; and b) coordinate system for the mathematical model.

maximize the volumetric loading fraction by increasing the port-to-throat area ratio.

Aside from the three-dimensional internal ballistics codes such as the standard stability prediction [39] and the solid propellant performance [2–4], there are many industrial codes that still refer to parallel profiles (such as Culick's [10]) as a basis for design and analysis [40]. When parallel profiles are applied to tapered SRMs, the result is overprediction of the pressure drop by as much as 50 to 85% for taper angles as small as 1 deg. Such discrepancies can drastically alter motor case design requirements to the extent of compromising the structural integrity of the case or its components.

II. Mathematical Model

For academic reasons, the SRM is characterized as a cylindrical, circular-port duct with a circumferential porous surface canted at an angle α. Our model in Fig. 1a incorporates both the nontapered and tapered geometries. This enables us to account for the bulk flow originating from the nontapered section of the motor. The origin for the coordinate system is placed at the interface where $\bar{z}$ and $\bar{r}$ denote the axial and radial coordinates, respectively (see Fig. 1b). The nontapered section of the cylindrical motor has dimensions of length L_0 and radius R_0. The gases are injected perpendicularly to the tapered surface. To satisfy mass conservation, the injected gases are forced to turn and merge with the bulk flow emerging from the parallel segment. The streamline behavior can be seen in Fig. 1a.

A. Governing Equations

In this problem, vorticity is produced at the surface as a result of the interaction between the injected fluid and the axial pressure gradient; one may begin by obtaining the required form of the vorticity. Furthermore, the flow can be taken to be 1) axisymmetric, 2) inviscid, 3) incompressible, 4) rotational, and 5) nonreactive. In accordance with the stated assumptions, the kinematic equations of motion can be written in scalar notation. In the interest of clarity, these are

$$\bar{u}_r \frac{\partial \bar{u}_r}{\partial \bar{r}} + \bar{u}_z \frac{\partial \bar{u}_r}{\partial \bar{z}} = -\frac{1}{\rho}\frac{\partial \bar{p}}{\partial \bar{r}} \tag{1}$$

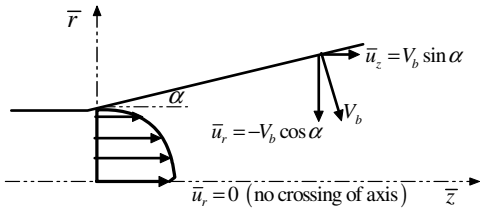

Fig. 2 Schematic of physical boundary conditions.

$$\bar{u}_r \frac{\partial \bar{u}_z}{\partial \bar{r}} + \bar{u}_z \frac{\partial \bar{u}_z}{\partial \bar{z}} = -\frac{1}{\rho}\frac{\partial \bar{p}}{\partial \bar{z}} \tag{2}$$

$$\bar{\Omega} = \bar{\Omega}_\theta = \frac{\partial \bar{u}_r}{\partial \bar{z}} - \frac{\partial \bar{u}_z}{\partial \bar{r}} = -\frac{1}{\bar{r}}\frac{\partial^2 \bar{\psi}}{\partial \bar{z}^2} - \frac{\partial}{\partial \bar{r}}\left(\frac{1}{\bar{r}}\frac{\partial \bar{\psi}}{\partial \bar{r}}\right) \tag{3}$$

where

$$\bar{u}_r = -\frac{1}{\bar{r}}\frac{\partial \bar{\psi}}{\partial \bar{z}}; \qquad \bar{u}_z = \frac{1}{\bar{r}}\frac{\partial \bar{\psi}}{\partial \bar{r}} \tag{4}$$

B. Boundary Conditions

While it is apparent that a radial velocity component exists at the interface, one should note that it does not contribute to the mass crossing into the tapered region; hence, it is not required to obtain a solution in the tapered domain (see Fig. 2). The key constraints consist of the following: 1) the axial inflow condition arising from mass balance across the taper interface (accounting for the bulk flow from the parallel portion of the motor); 2) no flow across the centerline; and 3) uniform, orthonormal injection at the burning surface. Mathematically, the boundary conditions can be evaluated and expressed as

$$\begin{cases} \bar{z} = 0, & \forall\ \bar{r}, & \bar{u}_z = \pi V_b (L_0/R_0)\cos(\frac{1}{2}\pi \bar{r}^2/R_0^2) \\ \bar{r} = \bar{r}_s, & \forall\ \bar{z}, & \bar{u}_z = V_b \sin\alpha \\ \bar{r} = \bar{r}_s, & \forall\ \bar{z}, & \bar{u}_r = -V_b \cos\alpha \\ \bar{r} = 0, & \forall\ \bar{z}, & \bar{u}_r = 0 \end{cases} \tag{5}$$

where V_b is the injection velocity at the burning surface.

C. Normalization

Normalization of the variables associated with the mathematical model provides a descriptive and compact solution. One may set

$$r = \frac{\bar{r}}{R_0}; \qquad z = \frac{\bar{z}}{R_0}; \qquad L = \frac{L_0}{R_0}; \qquad \nabla = R_0 \bar{\nabla} \tag{6}$$

$$u_r = \frac{\bar{u}_r}{V_b}; \qquad u_z = \frac{\bar{u}_z}{V_b}; \qquad p = \frac{\bar{p}}{\rho V_b^2} \tag{7}$$

$$\psi = \frac{\bar{\psi}}{R_0 V_b}; \qquad \Omega = \frac{R_0 \bar{\Omega}}{V_b} \tag{8}$$

Normalizing the equations and boundary conditions, it follows that

$$\begin{cases} u_r = -\dfrac{1}{r}\dfrac{\partial \psi}{\partial z} \\ u_z = \dfrac{1}{r}\dfrac{\partial \psi}{\partial r} \end{cases} \qquad \begin{cases} u_r \dfrac{\partial u_r}{\partial r} + u_z \dfrac{\partial u_r}{\partial z} = -\dfrac{\partial p}{\partial r} \\ u_r \dfrac{\partial u_z}{\partial r} + u_z \dfrac{\partial u_z}{\partial z} = -\dfrac{\partial p}{\partial z} \\ \dfrac{\partial^2 \psi}{\partial r^2} - \dfrac{1}{r}\dfrac{\partial \psi}{\partial r} + \dfrac{\partial^2 \psi}{\partial z^2} + \Omega_\theta = 0 \end{cases}$$

radial momentum

axial momentum

vorticity equation

$$\begin{cases} z = 0, & \forall\ r, & u_z = L\pi \cos(\frac{1}{2}\pi r^2) \\ r = r_s, & \forall\ z, & u_z = \sin\alpha \\ r = r_s, & \forall\ z, & u_r = -\cos\alpha \\ r = 0, & \forall\ z, & u_r = 0 \end{cases} \tag{9}$$

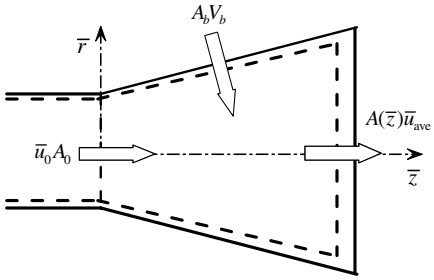

Fig. 3 Mass balance over a tapered segment.

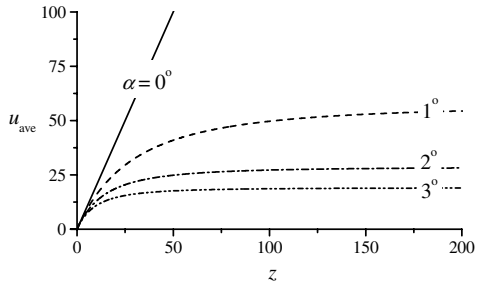

Fig. 4 Axial variation of average velocity for $L = 0$.

D. Average Velocity

The geometry is based on the cylindrical coordinate system (depicted in Fig. 3) where $\bar{z}$ is the dimensional axial coordinate and $\bar{r}$ is the dimensional radial coordinate. The area of the sloped surface is calculated to be

$$A_b = 2\pi\bar{z}\sec\alpha(R_0 + \tfrac{1}{2}\bar{z}\tan\alpha) \tag{10}$$

Also, the tapered chamber cross-sectional area is

$$A(\bar{z}) = \pi(R_0 + \bar{z}\tan\alpha)^2 \tag{11}$$

The inflow cross-sectional area at the interface of the tapered and straight portions of the chamber is given by

$$A_0 = \pi R_0^2 \tag{12}$$

As a result of a mass balance in the straight segment of the chamber, the average inflow velocity becomes

$$\bar{u}_0 = (2L_0/R_0)V_b \tag{13}$$

Here L_0 is termed the bulk flow parameter because it is directly proportional to the average velocity at the entrance to the tapered domain. Because of mass conservation, the cross-sectional average velocity of the fluid at any axial location $\bar{z}$ may be expressed by

$$\bar{u}_{ave}(\bar{z}) = \frac{A_0\bar{u}_0 + A_bV_b}{A(\bar{z})} \tag{14}$$

By substituting Eqs. (10–13), the average normalized velocity becomes

$$u_{ave}(z) = 2\frac{L + z\sec\alpha(1 + \frac{1}{2}z\tan\alpha)}{(1 + z\tan\alpha)^2} \tag{15}$$

For the case $\alpha = 0$, Eq. (15) reduces to

$$u_{ave}(z) = 2(z + L) \tag{16}$$

This relation describes the bulk flow in a straight circular-port motor. To determine the behavior of the gases when sufficiently removed from the head end, one may manipulate Eq. (15) and compute the limit of the resulting expression. One gets

$$u_{ave}(z) = 2\left(\frac{1}{z} + \tan\alpha\right)^{-2}\left[\frac{L}{z} + \sec\alpha\left(\frac{1}{z} + \frac{\tan\alpha}{2}\right)\right] \tag{17}$$

The limit at $z \to \infty$ furnishes

$$\lim_{z\to\infty} u_{ave}(z) = \csc\alpha \tag{18}$$

From Eq. (18), it can be seen that the velocity in a tapered chamber converges to a constant value as the motor length becomes large. This behavior is illustrated in Fig. 4. Thus, it can be seen that the flow cannot continue to accelerate due to the gradual increase in cross-sectional area. This is contrary to the case of a parallel port motor where the velocity continues to increase in the downstream direction. Typically, combined motor configurations have a straight cylinder immediately followed by a tapered segment. In light of this, it is physically impossible for the velocity of the gases to increase beyond the limiting value prescribed by the tapered geometry. Mass conservation requires that the average velocity throughout the parallel segment of the motor remains less than or equal to the limiting value. This is equivalent to setting

$$u_{ave}(z)|_{\alpha=0\ \deg} \le u_{ave}(\infty) \quad \text{or} \quad z \le \tfrac{1}{2}\csc\alpha - L \tag{19}$$

With subsequent manipulation [and expressing Eq. (19) in dimensional variables], one obtains

$$\bar{z} \le \tfrac{1}{2}R_0/\alpha - L_0 \tag{20}$$

where the small angle approximation $\sin\alpha \simeq \alpha$ is used. The geometric parameters of the motors must be chosen such that Eq. (20) is satisfied. Compliance with this criterion ensures a valid solution.

E. Stream Function Along the Burning Surface

A crucial component to the formulation of the flowfield under study is the development of the stream function at the simulated burning surface. It is clear that the behavior of the stream function depends on the angular orientation of the propellant surface. As shown in Fig. 5, the normalized variables along the burning surface can be readily determined to be

$$z = s\cos\alpha \tag{21}$$

$$r_s = 1 + s\sin\alpha = 1 + z\tan\alpha \tag{22}$$

$$u_{r,s} = -\cos\alpha, \qquad u_{z,s} = \sin\alpha \tag{23}$$

As a result, the directional derivative assumes the form

$$\frac{\mathrm{d}\psi_s}{\mathrm{d}s} = \frac{\partial\psi_s}{\partial r}\frac{\mathrm{d}r}{\mathrm{d}s} + \frac{\partial\psi_s}{\partial z}\frac{\mathrm{d}z}{\mathrm{d}s} = \frac{\partial\psi_s}{\partial r}\sin\alpha + \frac{\partial\psi_s}{\partial z}\cos\alpha \tag{24}$$

The stream function relations at the simulated burning surface can be defined as

$$\frac{\partial\psi_s}{\partial r} = r_s u_{z,s}, \qquad \frac{\partial\psi_s}{\partial z} = -r_s u_{r,s} \tag{25}$$

Then, insertion of the stream function definitions into Eq. (24) yields

$$\frac{\mathrm{d}\psi_s}{\mathrm{d}s} = r_s(\sin^2\alpha + \cos^2\alpha) = 1 + s\sin\alpha \tag{26}$$

Subsequent integration of Eq. (26) renders $\psi_s(s) = s(1+$

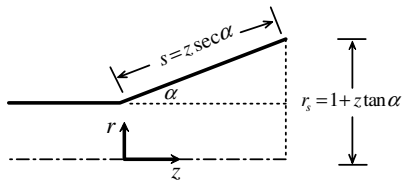

Fig. 5 Schematic of burning surface quantities.

$\frac{1}{2}s\sin\alpha) + C$, hence

$$\psi_s(z) = z\sec\alpha(1+\tfrac{1}{2}z\tan\alpha) + C \tag{27}$$

where C is a constant that may be determined from the boundary condition, $\psi_s(0) = L$. Application of this constraint gives

$$\psi_s(z) = z\sec\alpha(1+\tfrac{1}{2}z\tan\alpha) + L \tag{28}$$

It is to be noted that with the above expressions, the average velocity reduces to

$$u_{\text{ave}}(z) = 2\frac{\psi_s}{r_s^2} = 2\frac{z\sec\alpha(1+\frac{1}{2}z\tan\alpha)+L}{(1+z\tan\alpha)^2} \tag{29}$$

F. Axial Pressure Gradient

The axial pressure gradient is deemed to be the primary source of vorticity. As a result, we may begin by expressing the axial variation of pressure in the form of Bernoulli's equation as

$$p(z) = p_0 - \tfrac{1}{2}u_{\max}^2(z) \tag{30}$$

It may be useful to recall that the pressure variation is sensitive to the shape of the axial velocity profile. One should also note that the shape of the profile changes at each axial location and that the maximum velocity is unknown. It will be therefore helpful to define an expression that captures the effect of profile variation in z as the gases make their way toward the exit plane. This will be accomplished by defining the ratio of maximum-to-average velocities as

$$\beta(z) = \frac{u_{\max}(z)}{u_{\text{ave}}(z)} \tag{31}$$

The form of $\beta(z)$ will be later determined from imposition of the no-slip requirement at the burning surface. By substituting Eq. (31) into Eq. (30), one is left with

$$p = p_0 - \tfrac{1}{2}\beta^2 u_{\text{ave}}^2(z) \tag{32}$$

The pressure gradient is determined along the simulated burning surface by evaluating the derivative of Eq. (32). The result is

$$\frac{\partial p}{\partial z} = -\beta^2(z)u_{\text{ave}}(z)\left[\frac{\mathrm{d}u_{\text{ave}}(z)}{\mathrm{d}z} + \frac{u_{\text{ave}}(z)}{\beta(z)}\frac{\mathrm{d}\beta(z)}{\mathrm{d}z}\right] \tag{33}$$

Next, the axial derivative of the average velocity may be obtained from Eq. (29), namely,

$$\frac{\mathrm{d}u_{\text{ave}}}{\mathrm{d}z} = 2\frac{\sec\alpha}{r_s} - 4\frac{\psi_s\tan\alpha}{r_s^3} \tag{34}$$

Substituting Eq. (34) into Eq. (33) and simplifying, it follows that

$$\frac{\partial p}{\partial z} = -4\beta^2\frac{\psi_s\sec\alpha}{r_s^3}\left[1 - 2\frac{\psi_s\sin\alpha}{r_s^2} + \frac{\psi_s\cos\alpha}{r_s}\left(\frac{\beta'}{\beta}\right)\right]; \quad \beta' = \frac{\mathrm{d}\beta}{\mathrm{d}z} \tag{35}$$

G. Surface Vorticity

Having determined the relationship between stream function and pressure, the momentum equation for steady, inviscid flows may be evaluated at the surface. To begin, one may recall the normalized form of Euler's equation,

$$\tfrac{1}{2}\nabla(\boldsymbol{u}\cdot\boldsymbol{u}) - \boldsymbol{u}\times(\nabla\times\boldsymbol{u}) = -\nabla p \quad \text{or} \quad \boldsymbol{u}\times\boldsymbol{\Omega} = \nabla(p + \tfrac{1}{2}\boldsymbol{u}\cdot\boldsymbol{u}) \tag{36}$$

The normalized velocity at the simulated burning surface can be expressed in terms of the taper angle via

$$\boldsymbol{u}_s = -\cos\alpha\boldsymbol{e}_r + \sin\alpha\boldsymbol{e}_z \tag{37}$$

Evaluating the expression at the surface by substitution of Eq. (37) into Eq. (36) gives

$$\boldsymbol{u}\times\boldsymbol{\Omega} = -\Omega_s(\sin\alpha\boldsymbol{e}_r + \cos\alpha\boldsymbol{e}_z) = -\Omega_s\hat{\boldsymbol{s}} \tag{38}$$

Here $\hat{\boldsymbol{s}}$ represents the unit vector parallel to the burning surface. The corresponding pressure gradient can be expressed as

$$\frac{\mathrm{d}p}{\mathrm{d}s}\hat{\boldsymbol{s}} = \left(\frac{\partial p}{\partial r}\frac{\mathrm{d}r}{\mathrm{d}s} + \frac{\partial p}{\partial z}\frac{\mathrm{d}z}{\mathrm{d}s}\right)\hat{\boldsymbol{s}} = \left(\frac{\partial p}{\partial r}\sin\alpha + \frac{\partial p}{\partial z}\cos\alpha\right)\hat{\boldsymbol{s}} \tag{39}$$

At the surface, $\nabla(\boldsymbol{u}\cdot\boldsymbol{u}) = 0$; this enables us to equate Eqs. (38) and (39). At the outset, we collect

$$\Omega_s = -\frac{\partial p}{\partial r}\sin\alpha - \frac{\partial p}{\partial z}\cos\alpha = -\frac{\partial p}{\partial z}\cos\alpha + \mathcal{O}(\sin\alpha) \tag{40}$$

Note that, with values of α between 1 and 3 deg, the term containing $\sin\alpha$ has been suppressed. Finally, the surface vorticity can be expressed as

$$\Omega_s = 4\beta^2\frac{\psi_s}{r_s^3}\left[1 - 2\frac{\psi_s\sin\alpha}{r_s^2} + \frac{\psi_s\cos\alpha}{r_s}\left(\frac{\beta'}{\beta}\right)\right] \tag{41}$$

At this juncture, one may seek a relationship that permits satisfying the steady vorticity transport equation given by the curl of Eq. (36), specifically, $\nabla\times(\boldsymbol{u}\times\boldsymbol{\Omega}) = 0$. This is identically satisfied when the vorticity and stream function are proportional via $\Omega/r \propto \psi$. Knowing that the value of ψ must remain constant along a streamline, one may equate ψ to ψ_s, its value at the tapered surface; it follows that

$$\frac{\Omega}{r} = \frac{\Omega_s}{r_s} \quad \text{or} \quad \Omega = \frac{r}{r_s}\Omega_s \tag{42}$$

Substituting Eq. (41) into (42) yields

$$\Omega(r,z) = 4\beta^2 r\frac{\psi}{r_s^4}\left[1 - 2\frac{\psi\sin\alpha}{r_s^2} + \frac{\psi\cos\alpha}{r_s}\left(\frac{\beta'}{\beta}\right)\right] \tag{43}$$

This key relation is shown on Fig. 6.

III. Approximate Solutions

With a complete formulation for the chamber vorticity, a partial, nonlinear differential equation that governs the flow is at hand. This can be obtained by substituting Eq. (43) into Eq. (9); the resulting vorticity equation turns into:

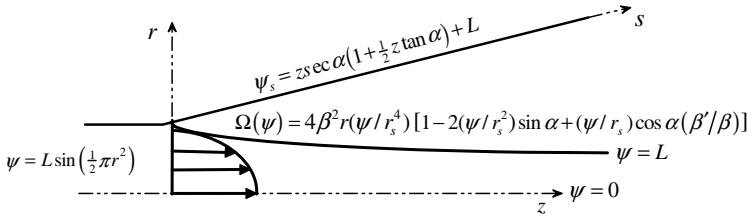

Fig. 6 Mathematical model depicting surface vorticity and stream function.

$$\frac{\partial^2\psi}{\partial r^2}-\frac{1}{r}\frac{\partial\psi}{\partial r}+\frac{\partial^2\psi}{\partial z^2}=-4\beta^2r^2\frac{\psi}{r_s^4}\left[1-2\frac{\psi\sin\alpha}{r_s^2}+\frac{\psi\cos\alpha}{r_s}\left(\frac{\beta'}{\beta}\right)\right] \tag{44}$$

By numerical methods, Clayton [40] notes that β' and $\partial^2\psi/\partial z^2$ are small quantities. Clayton's observations may be verified using a scaling analysis. Considering that

$$\frac{\partial^2\psi}{\partial z^2}=\frac{\partial(ru_r)}{\partial z} \tag{45}$$

one may recall that u_r is independent of z in the straight circular-port, thus causing Eq. (45) to vanish at leading order. It is clear that the presence of small taper will not affect the size of this term, given the magnitude of $\sin\alpha$. Henceforth, it is posited that the axial derivatives are of small magnitude and can be neglected in the tapered domain. Using Clayton's arguments, Eq. (44) is reduced to

$$\frac{\partial^2\psi}{\partial r^2}-\frac{1}{r}\frac{\partial\psi}{\partial r}=-4\beta^2r^2\frac{\psi}{r_s^4}\left(1-2\frac{\psi\sin\alpha}{r_s^2}\right) \tag{46}$$

The two boundary conditions that are required to solve Eq. (44) are given by

$$\psi(0,z)=0,\qquad \psi(r_s,z)=\psi_s \tag{47}$$

With a nonlinear partial differential equation at hand, the method of regular perturbations may be applied. In concert with such a methodology, the stream function and velocities may be expanded in the form

$$\psi=\psi_0+\varepsilon\psi_1+\mathcal{O}(\varepsilon^2) \tag{48}$$

$$\boldsymbol{u}=\boldsymbol{u}_0+\varepsilon\boldsymbol{u}_1+\mathcal{O}(\varepsilon^2) \tag{49}$$

$$\beta=\beta_0+\varepsilon\beta_1+\mathcal{O}(\varepsilon^2) \tag{50}$$

where the perturbation parameter is due to the small taper angle, namely,

$$\varepsilon\equiv\sin(\alpha) \tag{51}$$

A solution may be obtained by substituting Eqs. (48–52) into Eq. (46). The resulting expression may then be expanded into a linear sequence of ordinary differential equations.

A. Leading-Order Solution

At leading order, one obtains

$$\frac{\partial^2\psi_0}{\partial r^2}-\frac{1}{r}\frac{\partial\psi_0}{\partial r}+\frac{4\beta_0^2r^2}{r_s^4}\psi_0=0 \tag{52}$$

This is a simple, second-order, linear differential equation with the general solution

$$\psi_0(r,z)=C_1\cos\left(\beta_0\frac{r^2}{r_s^2}\right)+C_2\sin\left(\beta_0\frac{r^2}{r_s^2}\right) \tag{53}$$

Straightforward evaluation of Eq. (53) at the assigned boundary conditions gives

$$\psi_0(r,z)=\psi_s\sin\left(\beta_0\frac{r^2}{r_s^2}\right) \tag{54}$$

where

$$\psi_s(z)=z\sec\alpha(1+\tfrac{1}{2}z\tan\alpha)+L\quad\text{and}\quad\beta_0=\tfrac{1}{2}\pi \tag{55}$$

It should be noted that at $L=\alpha=0$, one recovers

$$\psi_0(r,z)=z\sin(\beta_0r^2) \tag{56}$$

Equation (56) reproduces Culick's profile [10] for flow in an internal burning cylinder. The leading-order solution expressed by Eq. (54) may be referred to as an extended version of Culick's profile. This form is a result of the additional bulk flow caused by the increased surface area.

B. First-Order Solution

At first order, one obtains the following ordinary differential equation:

$$\frac{\partial^2\psi_1}{\partial r^2}-\frac{1}{r}\frac{\partial\psi_1}{\partial r}+\frac{4\beta_0^2r^2}{r_s^4}\psi_1+\frac{8r^2\beta_0\beta_1}{r_s^4}\psi_0-\frac{8r^2\beta_0^2}{r_s^6}\psi_0^2=0 \tag{57}$$

with

$$\psi_1(0)=0,\qquad \psi_1(r_s)=0 \tag{58}$$

Applying these boundary conditions, one obtains

$$\psi_1(r,z)=\frac{\psi_s}{3r_s^2}\left[3\psi_s+\psi_s\cos\left(2\beta_0\frac{r^2}{r_s^2}\right)-2\psi_s\sin\left(\beta_0\frac{r^2}{r_s^2}\right)-4\psi_s\cos\left(\beta_0\frac{r^2}{r_s^2}\right)+3\beta_1r^2\cos\left(\beta_0\frac{r^2}{r_s^2}\right)\right] \tag{59}$$

The first-order velocity ratio β_1 must be determined such that the no-slip condition is satisfied along the tapered surface. This can be written as

$$\nabla\psi_s\cdot\hat{\boldsymbol{s}}=\nabla\psi\cdot\hat{\boldsymbol{s}}=0 \tag{60}$$

therefore,

$$\frac{\partial\psi}{\partial r}\cos\alpha+\frac{\partial\psi}{\partial z}\sin\alpha=(\psi_0+\varepsilon\psi_1)_r\cos\alpha+(\psi_0+\varepsilon\psi_1)_z\sin\alpha=0 \tag{61}$$

Noting that ψ_0 already satisfies the no-slip condition at the wall, we recover

$$\frac{\partial\psi_1}{\partial r}\cos\alpha+\frac{\partial\psi_1}{\partial z}\sin\alpha=0 \tag{62}$$

Again, it can be seen that the term containing $\sin\alpha$ is negligibly small, being of $\mathcal{O}(\varepsilon)$. Setting Eq. (62) equal to zero and evaluating the resulting expression at the tapered surface, one obtains

$$\beta_1=\frac{4\psi_s}{3r_s^2} \tag{63}$$

The required forms of the leading and first-order velocity ratios, β_0 and β_1, are presently known.

C. Velocity, Pressure, and Vorticity

With the proper form of the stream function available, it is now possible to evaluate the physical characteristics of the flowfield. For simplicity, we define

$$\eta=\beta_0\frac{r^2}{r_s^2} \tag{64}$$

The leading and first-order stream functions become

$$\psi_0(r,z)=\psi_s\sin\eta \tag{65}$$

and

$$\psi_1(r,z)=\frac{\psi_s}{3r_s^2}[3\psi_s+\psi_s\cos(2\eta)-2\psi_s\sin\eta-4\psi_s\cos\eta+3\beta_1r^2\cos\eta] \tag{66}$$

The radial and axial velocities are

$$\begin{cases} u_r = u_{r,0} + \varepsilon u_{r,1} + \mathcal{O}(\varepsilon^2) \\ u_z = u_{z,0} + \varepsilon u_{z,1} + \mathcal{O}(\varepsilon^2) \end{cases} \tag{67}$$

Using the relationship between the velocity and stream function, the leading and first-order axial velocity profiles are expressed by

$$u_{z,0} = \frac{1}{r}\frac{\partial \psi_0}{\partial r} = \frac{2\beta_0 \psi_s}{r_s^2}\cos\eta = \beta_0 u_{\text{ave}}\cos\eta \tag{68}$$

and

$$u_{z,1} = \frac{1}{r}\frac{\partial \psi_1}{\partial r} = \frac{\psi_s}{3r_s^4}\Big[\Big(6\beta_1 r_s^2 - 4\beta_0\psi_s\Big)\cos\eta + \beta_0(8\psi_s - 6\beta_1 r^2)\sin\eta - 4\beta_0\psi_s\sin(2\eta)\Big] \tag{69}$$

which can be written very conveniently in terms of the average velocity as

$$u_{z,1} = \tfrac{1}{3}u_{\text{ave}}^2[(2-\beta_0)\cos\eta + 2(\beta_0 - \eta)\sin\eta - \beta_0\sin(2\eta)] \tag{70}$$

Because the variation of the chamber radius is of $\mathcal{O}(\sin\alpha)$, r_s, albeit function of z, is treated as a constant. With this in mind, the leading-order radial velocity can be expressed as

$$u_{r,0} = -\frac{1}{r}\frac{\partial \psi_0}{\partial z} = -\frac{r_s}{r}\sec\alpha\sin\eta \tag{71}$$

The first-order radial velocity component becomes

$$u_{r,1} = -\frac{1}{r}\frac{\partial \psi_1}{\partial z} = -\frac{1}{r}\frac{\partial \psi_1}{\partial \psi_s}\frac{\mathrm{d}\psi_s}{\mathrm{d}z} - \frac{1}{r}\frac{\partial \psi_1}{\partial r_s}\frac{\mathrm{d}r_s}{\mathrm{d}z} = -\frac{1}{r}\frac{\partial \psi_1}{\partial \psi_s}\frac{\mathrm{d}\psi_s}{\mathrm{d}z} - \frac{\tan\alpha}{r}\frac{\partial \psi_1}{\partial r_s} = -\frac{\partial \psi_1}{\partial \psi_s}\frac{\mathrm{d}\psi_s}{\mathrm{d}z} + \mathcal{O}(\varepsilon) \tag{72}$$

At first order, the $\mathcal{O}(\varepsilon)$ terms in $u_{r,1}$ become $\mathcal{O}(\varepsilon^2)$; therefore, we only need to evaluate the first term in Eq. (72), specifically,

$$u_{r,1} = -\frac{2\psi_s\sec\alpha}{3rr_s}\left[3 + \cos(2\eta) - 2\sin\eta - 4\cos\eta + 4\frac{r^2}{r_s^2}\cos\eta\right] + \mathcal{O}(\varepsilon) \tag{73}$$

$$= -\frac{r_s}{3r}u_{\text{ave}}\sec\alpha[3 + \cos(2\eta) - 2\sin\eta - 4\cos\eta + (8/\pi)\,\eta\cos\eta] + \mathcal{O}(\varepsilon) \tag{74}$$

From the velocity profiles, the spatial variation of the pressure can be ascertained. The substitution of the velocity components into the z- and r-momentum equations yields

$$\frac{\partial p_0}{\partial z} = -\frac{\pi^2}{4}\frac{\psi_s\sec\alpha}{r_s^3} \tag{75}$$

and so, by keeping r_s constant,

$$\frac{\partial p_0}{\partial r} = -\frac{\sec^2\alpha}{r^3}\Big\{r_s^2[\cos(2\eta) - 1] + 2\beta_0 r^2\sin(2\eta)\Big\} \tag{76}$$

By integrating and combining Eqs. (75) and (76), one is able to produce the spatial variation of the pressure that satisfies both momentum equations. By inspection, one concludes that the radial component of pressure is of marginal importance, being of $\mathcal{O}(\sin^2\alpha)$. At leading order, Eq. (75) may be integrated to obtain

$$p(z) = -\frac{\pi^2}{2}\frac{z\sec\alpha}{r_s^4}(z\sec\alpha + 2L) + p_{\text{Culick}} \tag{77}$$

where $p(0,0) = p_{\text{Culick}} = -\frac{1}{2}L^2\pi^2$ stems from the head-end boundary condition. Setting $\Delta p = p - p_{\text{Culick}}$, one may express the leading-order expression for the pressure drop as

$$\Delta p_0 = -\frac{\pi^2}{2}\frac{z\sec\alpha}{r_s^4}(z\sec\alpha + 2L) = -\frac{\pi^2}{2}\frac{z\sec\alpha}{(1 + z\tan\alpha)^4}(z\sec\alpha + 2L) \tag{78}$$

Knowing that r_s is treated as a constant for first-order approximations, it may be argued that some error may be incurred as a result of performing multiple differentiation and integration operations that neglect the axial dependence of the radius. Also, the evaluation of the derivatives and subsequent integration of the resulting expression produce higher-order terms that, for purposes of retrieving a leading-order solution, may be dismissed. In an attempt to improve accuracy, one may seek a higher-order correction for the pressure drop. This higher-order correction accounts for the second-order axial derivative of the stream function as well as the variation of r_s with axial distance. Evidently, this variation becomes more significant at larger taper angles. Our second-order accurate approximation for the pressure drop can be expressed as

$$\Delta p_1(z) = -\frac{\pi^2}{2}\frac{z\sec\alpha}{r_s^4}(z\sec\alpha + 2L) - \varepsilon\frac{z\sec\alpha}{18r_s^8} \times \{4(\pi-4)^2 z^3\sec^3\alpha + z^2\sec^2\alpha\Big[16(\pi-4)^2 L + 9\pi^2 r_s^4\Big] + 3Lz\sec\alpha\Big[8(\pi-4)^2 L + 3\pi^2 r_s^4\Big] + 16(\pi-4)^2 L^3\} \tag{79}$$

For $L = 0$, we recover

$$\Delta p_1(z) = -\frac{\pi^2}{2}\frac{z^2\sec^2\alpha}{r_s^4} - \varepsilon\frac{z^3\sec^3\alpha}{18r_s^8}\Big[4(\pi-4)^2 z\sec\alpha + 9\pi^2 r_s^4\Big] \tag{80}$$

In addition to the formulation of the velocity and pressure gradients, one may evaluate the vorticity. This can be accomplished via

$$\Omega_\theta(r,z) = \frac{1}{r}\left(\frac{\sec\alpha\tan\alpha}{r} - \frac{4r\psi_s}{r_s^4}\right)\sin\left(\beta_0\frac{r^2}{r_s^2}\right) \tag{81}$$

Each of the required flowfield characteristics particular to tapered cylindrical motors is now at hand. The effect of the bulk flow parameter will be examined along with the taper angle. One should note that this parameter is also the normalized chamber length $L = L_0/R_0$.

D. Ideal Momentum Thrust

In pursuit of an expression that reveals the response of the thrust to the taper angle, the axial momentum force, at any station z, may be calculated viz.

$$\bar{F} = 2\pi\rho V_b^2 R_0^2\int_0^{r_s} u_z^2 r\,\mathrm{d}r \tag{82}$$

Following the convention adopted in Eqs. (6) and (7), one can put

$$F(z) = 2\pi\int_0^{r_s} u_z^2 r\,\mathrm{d}r; \qquad F = \frac{\bar{F}}{\rho V_b^2 R_0^2} \tag{83}$$

It is informative to evaluate Eq. (83) using the average velocity. The corresponding thrust is simply

$$F_{\text{ave}}(z) = \frac{\pi[2L + z\sec\alpha(2 + z\tan\alpha)]^2}{(1 + z\tan\alpha)^2} \tag{84}$$

The actual thrust may be estimated from $F(z) = 2\pi\int_0^{r_s}(u_{z,0}^2 + 2\varepsilon u_{z,0}u_{z,1})r\,\mathrm{d}r = F_0(z) + \varepsilon F_1(z) + \ldots$; to first order, this expan-

sion yields

$$F(z) = \tfrac{1}{2}\pi^3(L + z\sec\alpha)^2 - \tfrac{1}{2}\pi^2\varepsilon(L + z\sec\alpha)[\tfrac{4}{9}(3\pi - 10) \times (L + z\sec\alpha)^2 + \pi z\sec\alpha(2L + z\sec\alpha)] + \ldots \quad (85)$$

Subsequently, for $L = 0$, one retrieves $F = \frac{1}{2}\pi^3 z^2\sec^2\alpha - \frac{1}{6}\pi^2(7\pi - \frac{40}{3})\varepsilon z^3\sec^3\alpha + \mathcal{O}(\varepsilon^2)$. The companion momentum correction coefficient may be calculated from $\lambda = F/F_{\text{ave}} = \lambda_0 + \varepsilon\lambda_1 + \mathcal{O}(\varepsilon^2)$. Based on Eqs. (84) and (85), one collects

$$\begin{cases} \lambda_0 = \dfrac{\pi^2}{8} + \dfrac{(21\pi - 40)\pi z\sec\alpha(2L + z\sec\alpha) + 4L^2(3\pi - 10)}{72(L + z\sec\alpha)} \\ \lambda_1 = \dfrac{\pi^2 z(2L + z\sec\alpha)}{8(z + L\cos\alpha)} + \dfrac{\pi z(z + 2L\cos\alpha)\sec^4\alpha[(21\pi - 40)z^2 + 2L(21\pi - 40)z\cos\alpha + 4L^2(3\pi - 10)]}{72(2L + z\sec\alpha)^2} \end{cases} \quad (86)$$

Finally, for $L = 0$, simple expressions are recovered, namely,

$$\begin{cases} \lambda_0 = \frac{1}{8}\pi^2 + \frac{1}{72}\pi(21\pi - 40)z\sec\alpha \\ \lambda_1 = \frac{1}{8}\pi^2 z\sec\alpha + \frac{1}{72}\pi(21\pi - 40)z^2\sec^2\alpha \end{cases} \quad (87)$$

The momentum correction coefficient reduces to a constant $\lambda = \frac{1}{8}\pi^2 \simeq 1.2337$ for the no taper case. It reaches a maximum value of 1.23546 at

$$z = \frac{200 - 105\pi + \sqrt{27200 - 31440\pi + 9009\pi^2}}{2(21\pi - 40)}\cot\alpha \simeq 0.0351868\cot\alpha \quad (88)$$

The behavior of the thrust force is more fully described in Sec. V.B.

IV. CFD Confirmation

A perturbation technique has enabled us to obtain closed-form approximations that describe the mean flowfield for the circular-port motor with tapered bore. A numerical simulation is now invoked to validate the analytical results and verify their assumptions and ranges of applicability which, so far, could only be estimated with asymptotics. In the interest of simplicity, a numerical simulation is performed with the use of a commercial code [41]; the purpose is to recreate the simulated environment evoked in deriving the analytical solutions.

A. Geometry and Meshing Scheme

The geometric models are created for taper angles ranging from 1 to 3 deg. The dimensions are chosen in accordance with the parameters used by the analytical model. The cylindrical motor is represented in three-dimensional space, and the gaseous mixture (assuming single phase) is injected across its simulated burning surface. A standard meshing scheme is employed with an interval size of 0.1.

B. Boundary and Operating Conditions

The reference pressure we use is the stagnation pressure at the head end of the chamber, specifically, the pressure at the origin. The working fluid is injected at velocities ranging from 0.1 to 1 m/s. These values of injection velocity ensure that the Mach number remains less than 0.3, hence justifying the incompressible flow condition used in the analytical treatment. The selection of the injection velocity follows from the experimental work of Brown, Dunlap, and coworkers [42,43]. This range may be sufficient in view of Clayton's CFD results [40]. These confirm that the taper profiles change minimally with increasing injection velocity provided that the wall injection Reynolds number, $Re = \rho V_b D/\mu$, falls between 10^2 and 10^4.

To capture coherent structures that correspond to our analytical solution, the numerical scheme that we adopt is based on the laminar model. We recognize, however, that the flowfield inside an actual SRM will be turbulent, particularly, in the downstream portions of an elongated chamber; this idea is nicely covered by Apte and Yang [44].

V. Results and Discussion

This section seeks to examine the dissimilarities that exist between the numerical and analytical cases presented earlier. With available information, one is able to determine the level of accuracy that is required and which physical parameters are most important. As noted by Clayton [40], the axial velocity profiles and the pressure drop are of paramount importance. However, the pursuit of a general expression that describes the flowfield in tapered geometry requires that certain terms be neglected during the derivation process. To validate the dismissal of these terms, the same problem is now solved numerically. In the forthcoming sections, the numerical results are compared to those found analytically.

A. Pressure Approximations

The slow increase in cross-sectional area in the axial direction acts to decrease the pressure drop by allowing a build up in local static pressure with the accompanying decrease in dynamic pressure. By comparison to Culick's solution in a straight circular-port motor [10], Figs. 7a and 7b illustrate that there are substantial decreases in the pressure drop at higher taper angles taken at a length-to-radius ratio of $z = 10$. The value of z corresponds to the maximum length of the tapered segment for a bulk flow value of zero. Recovering the error that has accrued as a result of the constant radius assumption and neglecting the second-order axial derivative requires the addition of a higher-order correction.

The behavior of the higher-order solution can be examined in Fig. 7b. The addition of the higher-order correction seems to have much more of an impact at higher taper angles and larger tapered domains; this trend suggests that the corrections are a requisite for analytical pressure predictions for these cases. Compared with the higher-order solution, the leading-order solution underpredicts the pressure drop at larger taper angles. In later portions of this work, the higher-order correction will prove to be essential for the validation of the mathematical model. It is clear that there is an overprediction in pressure drop. The error increases as the gases head toward the aft end. At the edge of the solution domain, the total pressure drop can be overpredicted by as much as 48 to 75% using the leading-order expression. The natural range for percent overprediction using the higher-order correction varies here between 24 and 52%. Obviously,

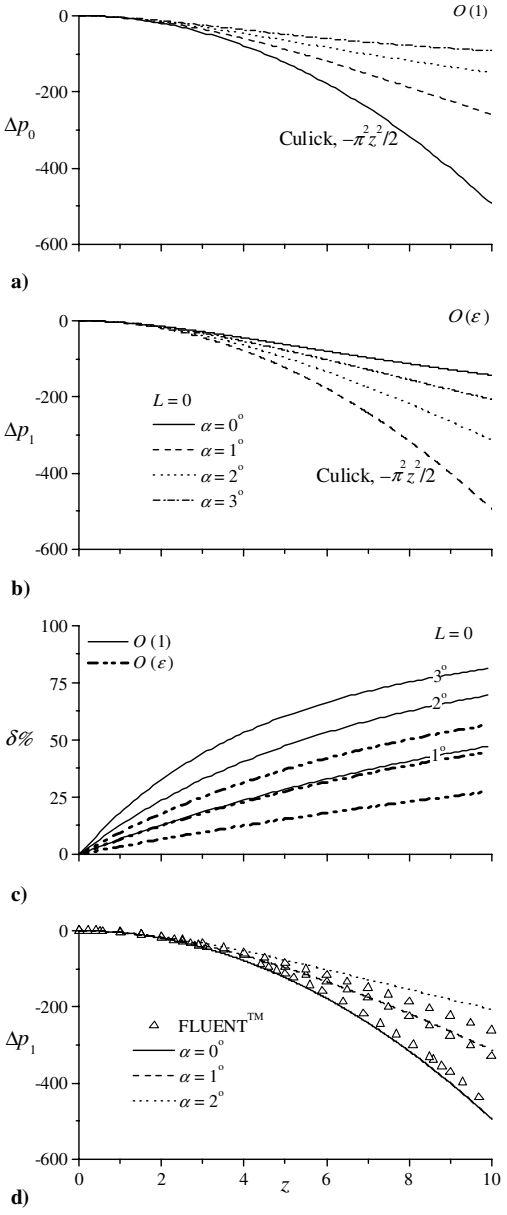

Fig. 7 Plots of a) leading-order and b) first-order approximations for several values of α. In c) the percent overprediction at several values of α and d) numerical vs first-order approximation are shown.

use of the leading-order solution to predict the total pressure drop is not sufficient.

B. Momentum Thrust Behavior

In Fig. 8, F, F_{ave}, and λ are shown at several taper angles and z; they are truncated in the streamwise direction when crossing their range of validity. The sensitivity of the momentum thrust to α seems to be consistent with that of the pressure drop. As the taper angle increases, continuity requires the average velocity to diminish along with the momentum thrust. It must be borne in mind, however, that this behavior corresponds to a steady-state, nozzleless, cold-flow solution that does not account for neutral, regressive, or progressive burning effects. The actual momentum thrust is slightly larger than the average value, as shown in Fig. 8b. Using $L = 0$, the momentum correction coefficient starts at $\frac{1}{8}\pi^2 \simeq 1.23370$, following Eq. (87); it increases to a maximum of 1.23546 at precisely $z = 0.0351868 \cot\alpha$, then decreases back to unity. The descent is more pronounced at higher taper angles for which the average velocity reaches its asymptotic limit more rapidly.

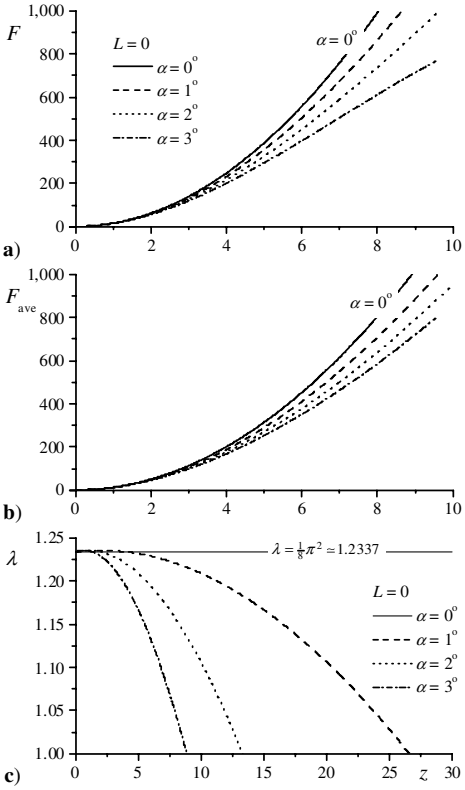

Fig. 8 Plots of a) actual thrust, b) average thrust and c) momentum correction coefficient, F/F_{ave} at several values of α.

C. Axial Velocity

One should recall that r_s was treated as a constant during the evaluation of the axial and radial velocity components. Consequently, it was expected that some error would be introduced into the solution. In Fig. 9, it can be observed that there exists no discernible pattern for the analytical profiles and their numerical counterparts. This may be attributed to the effects of curvature as well as the nonuniform 3-D computational grid used for the numerical model. As a result, the numerical solution is seen to slightly overshoot or undershoot the numerical solution at various axial locations. This rather random discrepancy is more noticeable further down the motor chamber; it may become non-negligible in very long motors.

One should note that the analytical solutions shown in Fig. 9 include higher-order corrections. Neglecting these higher-order terms leads to a grossly underpredicted maximum centerline velocity. From the graph, it can be inferred that the leading-order solution lacks valuable flow information and that the higher-order terms appear to be a requisite for accurate predictions in long chambers with large taper angles. The higher-order corrections seem to slowly recover the second-order axial derivative that was omitted in the basic solution. Clearly, Fig. 9 displays very good agreement between the analytical and numerical solutions.

D. Axial Derivatives

Our quest for an analytical, closed-form solution has required several assumptions. These assumptions have targeted several derivatives, namely 1) $\partial^2\psi/\partial z^2$ and 2) $\mathrm{d}\beta/\mathrm{d}z$. The magnitudes of the second-order axial derivatives of stream function have been extracted from the numerical solution and quantified along the axis. The second-order radial derivatives were also plotted for the purpose of comparing the two quantities. Figure 9a clearly depicts an oscillatory behavior as is typical of a small fluctuating quantity. These fluctuations remain insignificant, namely, of $\mathcal{O}(10^{-4})$ down the length of the chamber. In contrast, the radial derivatives shown in Fig. 10b exhibit magnitudes of $\mathcal{O}(1)$, thus justifying their retention in the analytical model.

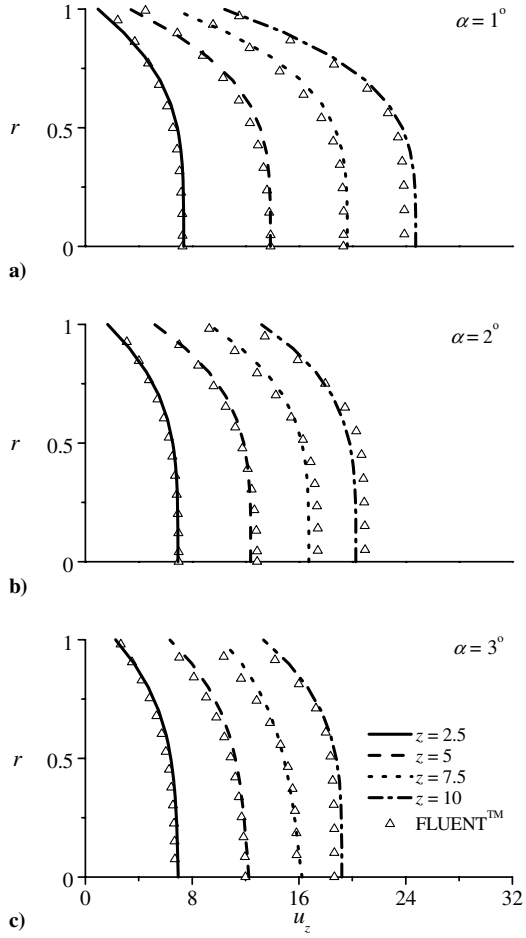

Fig. 9 CFD versus analytical velocity profiles at various axial locations for select taper angles.

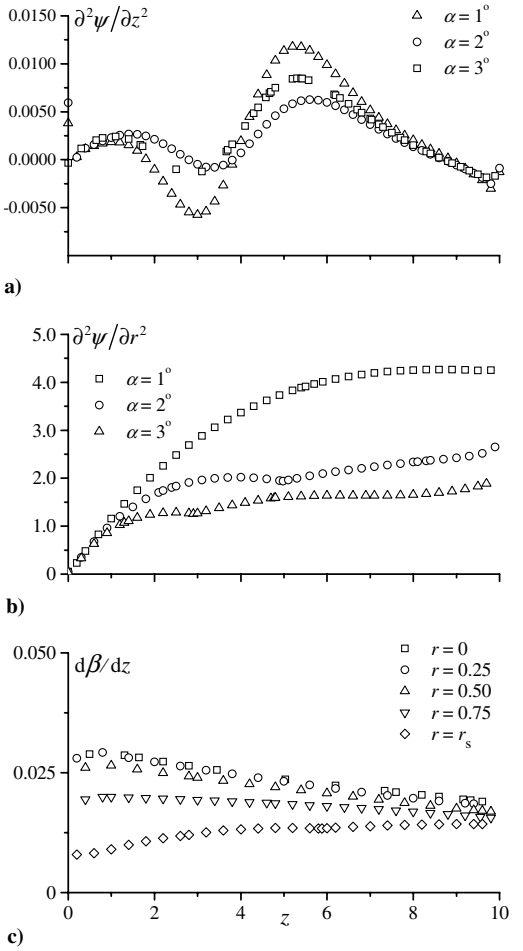

Fig. 10 Numerical axial derivative approximations from FLUENT™ shown at several taper angles.

Similarly, the magnitudes of the axial derivatives (described in Fig. 10c) for the velocity ratio are small enough that they would have no appreciable effect on the analytical solution. This plot shows the axial variation of $\mathrm{d}\beta/\mathrm{d}z$ at several radial locations for $\alpha = 3$ deg. From the graph, it can be inferred that the axial variation of each derivative dictates the shape of the velocity profile. For example, at $r = r_s$, the axial derivative slowly increases. One may recall that the velocity profile must adjust itself at each axial location to satisfy the no-slip requirement at the tapered surface. Bearing this in mind, it can be realized that the rate of change at the wall must increase due to the increased axial variation as the gases propagate down the chamber. At the axis of the chamber, one notices a decreasing derivative. This also indicates that the centerline velocity must decrease in the axial direction. From a physical standpoint, these changes must occur to satisfy mass conservation. The increasing rate of change at the wall works in conjunction with the decreasing rate of change at the axis to cause the profile to slowly relinquish its radial dependence with axial distance. Hence, the profile may evolve into a near constant shape over the cross-section for sufficiently long tapered domains.

VI. Limitations

For practical applications of the analytical solutions presented heretofore, one may be concerned with their parametric limitations. Previously, such limitations were explored by analytically predicting the behavior of the gases at an infinite distance from the head end. The results of this inquiry suggest that some relationships, guided by mass conservation, must be maintained between the geometric parameters. As shown in Sec. II.D, the pertinent relationship may be expressed as

$$\bar{z} \leq \frac{1}{2}\frac{R_0}{\alpha} - L_0 \tag{89}$$

This criterion was obtained using the average value of the velocity as opposed to the maximum centerline velocity. To determine a maximum range for which the analytical solutions remain applicable, one must calculate the maximum relative error between asymptotic predictions and numerical solutions. To do so, it is expedient to examine the asymptotic limit where the velocities in each chamber are at their maximum values; this can be accomplished, for instance, by comparing the centerline velocities predicted by numerics and those by asymptotics. For the nontapered segments, the relationship between centerline and average velocities can be easily found to be

$$u_{\max} = \tfrac{1}{2}\pi u_{\text{ave}} \tag{90}$$

By translating this result to the centerline velocity, the criteria that establish the upper limit of the solution domain may be extrapolated. One finds

$$\bar{z} \leq \frac{1}{\pi}\frac{R_0}{\alpha} - L_0 \tag{91}$$

Equation (91) can now be solved for $L_0 = 0$ to obtain the maximum *conservative* domain aspect ratio for a given taper angle. One finds

$$z_{\text{cons}} = \frac{\bar{z}_{\text{cons}}}{R_0} = \frac{1}{\pi\alpha} \tag{92}$$

It is our observation that, so long as $z \leq z_{\text{cons}}$, the percent error between numerics and asymptotics remains less than 1%. The conservative range represents a domain of asymptotic validity in

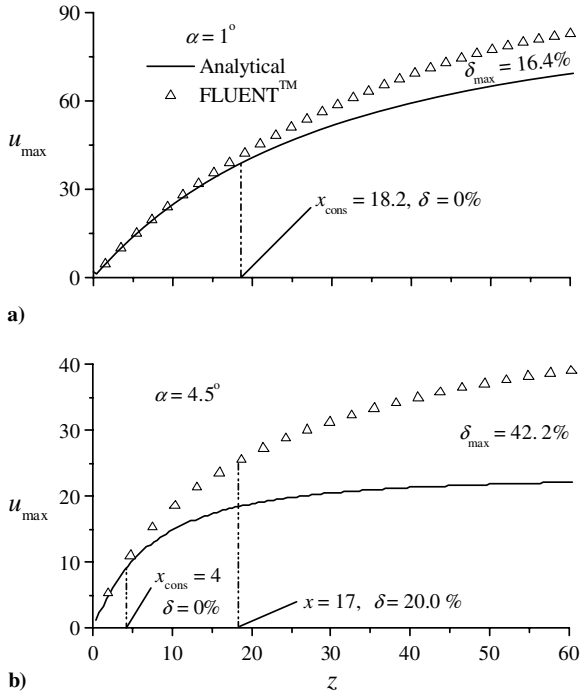

Fig. 11 Numerical and analytical approximations of the maximum (centerline) velocity with attendant relative error for two taper angles.

which the accrued error is virtually insignificant. By requiring a minimum chamber aspect ratio of 4 (lest edge effects become important), the maximum conservative taper angle for which an asymptotic solution would exhibit a smaller than 1% error can be readily calculated from Eq. (92). One finds the maximum conservative taper angle to be 4.5 deg. Therefore, a suitable range of tapers would be $0 < \alpha \leq 4.5$ deg.

Shown in Figs. 10a and 10b are the centerline velocities for $\alpha = 1$ and 4.5 deg, respectively. The behavior at $\alpha = 1$ deg is quite similar, although the range is different (due to the difference in geometries). In Fig. 11a, it is seen that the maximum percent deviation is about 16.4%. Here, the conservative range is $0 < z \leq 18.2$. As predicted, the two solutions (numerical and analytical) begin to diverge outside of the conservative domain.

For the case of the maximum taper angle, $\alpha = 4.5$ deg, the conservative range is reduced to $0 < z \leq 4$. The location at which a 20% discrepancy accrues between the two solutions is found to be approximately 17.0. For values greater than 17.0, the deviation begins to increase until it reaches a maximum value of 42.2%. The numerical cases shown here clearly support the analytical criterion within the conservative range. It may be inferred that the analytical solution exhibits a larger range of applicability for smaller taper angles.

For the idealized circular-port motor with very small taper (Fig. 11a), the maximum percent deviation δ is about 16.0% (at which point the error between numerics and asymptotics remains approximately constant as the solution levels off to a constant value). For such small taper, one may apply the analytical solution with minimal error, at least in theory, over an infinitely long domain. The range of aspect ratios for which relative discrepancies remain under 20% is generally much longer than those currently used in practice. In cold-flow models for SRMs, the present solution will remain within 20% of the numerical cases up to $z/z_{\text{cons}} \simeq 4$. In the interest of clarity, the key components of the solution are summarized in Table 1.

VII. Conclusions

In this study, we have presented an approximate solution for the mean flowfield in circular-port rocket motors with tapered bores. In pursuit of expressions that characterize the chamber pressure, mathematical operations were performed with the assumption that the distance from the centerline was constant, given its variation of $\mathcal{O}(\sin\alpha)$. Higher-order corrections were needed and these were found to compensate for the assumption of axial invariance of the chamber radius. Later, the higher-order corrections helped to recover the effect of the second-order axial derivative of the stream function.

Given the methodology to obtain the desired flowfield, the numerical simulation has been instrumental in substantiating the assumptions carried throughout the analytical derivation. Both theoretical avenues concur in that:

Table 1 Components of the canted Taylor–Culick profile

Variable	Equation
Stream function at canted surface	$\psi_s(z) = z\sec\alpha(1+\frac{1}{2}z\tan\alpha)+L$
Radius at canted surface	$r_s = 1+z\tan\alpha$
Vorticity at canted surface	$\Omega_s = 4\beta^2\frac{\psi_s}{r_s^3}\left[1-2\frac{\psi_s\sin\alpha}{r_s^2}+\frac{\psi_s\cos\alpha}{r_s}\left(\frac{\beta'}{\beta}\right)\right]$
Vorticity along streamline	$\Omega = 4\beta^2 r\frac{\psi}{r_s^4}\left[1-2\frac{\psi\sin\alpha}{r_s^2}+\frac{\psi\cos\alpha}{r_s}\left(\frac{\beta'}{\beta}\right)\right]$
Average velocity at flow cross section	$u_{\text{ave}} = 2\frac{\psi_s}{r_s^2} = 2\frac{z\sec\alpha(1+\frac{1}{2}z\tan\alpha)+L}{(1+z\tan\alpha)^2}$
Maximum-to-average velocity ratio	$\beta_0 = \frac{1}{2}\pi,\ \beta_1 = \frac{4\psi_s}{3r_s^2} = \frac{2}{3}u_{\text{ave}}$
Independent similarity variable	$\eta = \beta_0\frac{r^2}{r_s^2} = \frac{\pi r^2}{2(1+z\tan\alpha)^2}$
Stream function	$\psi_0 = \psi_s\sin\eta,\ \psi_1 = \frac{1}{6}u_{\text{ave}}\psi_s[3+\cos(2\eta)-2\sin\eta-4\cos\eta+(8/\pi)\eta\cos\eta]$
Axial velocity	$u_{z,0} = \frac{1}{2}\pi u_{\text{ave}}\cos\eta,\ u_{z,1} = \frac{1}{3}u_{\text{ave}}^2[(2-\frac{1}{2}\pi)\cos\eta+(\pi-2\eta)\sin\eta-\frac{1}{2}\pi\sin(2\eta)]$
Radial velocity	$u_{r,0} = -\frac{(1+z\tan\alpha)}{r}\sec\alpha\sin\eta,\ u_{r,1} = -\frac{u_{\text{ave}}}{3}\sec\alpha\frac{(1+z\tan\alpha)}{r}[3+\cos(2\eta)-2\sin\eta-4\cos\eta+(8/\pi)\eta\cos\eta]$
Leading-order axial pressure	$p = -\frac{\pi^2}{8}z\sec\alpha\frac{(z\sec\alpha+2L)}{(1+z\tan\alpha)^3}-\frac{\pi^2L^2}{2}$
Leading-order axial pressure drop	$\Delta p_0 = -\frac{\pi^2}{2}\frac{z\sec\alpha(z\sec\alpha+2L)}{(1+z\tan\alpha)^4}$
First-order axial pressure drop	$\Delta p_1 = -\frac{\pi^2}{2}\frac{z\sec\alpha}{r_s^4}(z\sec\alpha+2L)-\varepsilon\frac{z\sec\alpha}{18r_s^8}\{4(\pi-4)^2z^3\sec^3\alpha+z^2\sec^2\alpha[16(\pi-4)^2L+9\pi^2r_s^4]$ $+3Lz\sec\alpha[8(\pi-4)^2L+3\pi^2r_s^4]+16(\pi-4)^2L^3\}$
Average momentum thrust	$F_{\text{ave}} = \frac{\pi[2L+z\sec\alpha(2+z\tan\alpha)]^2}{(1+z\tan\alpha)^2}$
Actual momentum thrust	$F(z) = \frac{1}{2}\pi^3(L+z\sec\alpha)^2-\frac{1}{2}\pi^2\varepsilon(L+z\sec\alpha)[\frac{4}{9}(3\pi-10)(L+z\sec\alpha)^2+\pi z\sec\alpha(2L+z\sec\alpha)]$
Momentum correction coefficient for $L=0$	$\lambda_0 = \frac{1}{8}\pi^2+\frac{1}{72}\pi(21\pi-40)z\sec\alpha,\ \lambda_1 = \frac{1}{8}\pi^2z\sec\alpha+\frac{1}{72}\pi(21\pi-40)z^2\sec^2\alpha$
Limit on range of applicability	$z \leq \frac{1}{2}\csc\alpha - L$

1) The incorporation of the taper is required to avoid overpredicting the pressure drop.

2) The taper effect is more pronounced as the gases move away from the head end due to the increasing cross-sectional area.

3) Long motors with $L \geq 4$ experience reduced sensitivity to the taper angle. Smaller motors experience increased sensitivity.

4) The mean flow approaches its asymptotic limit in sufficiently long motors.

5) When modeling short motors or those with very small taper angles, ($0.5 \text{ deg} < \alpha \leq 1 \text{ deg}$), the leading-order solution is sufficient; however, for larger angles and longer motors, higher-order corrections become necessary.

6) The ideal momentum thrust diminishes at higher taper angles but increases with motor length until it reaches its asymptotic limit.

In closing, it may be worth mentioning that accurate matching of both numerical and analytical solutions requires that the motor parameters be chosen within specified limits. The corresponding criteria are discussed and shown to be practical. One shortcoming in the analytical solution is that it is long, albeit simple to implement and evaluate. In future work, we hope to extend this investigation to chambers with arbitrary cross section.

Acknowledgments

This project was partly sponsored by the National Science Foundation under Grant No. CMS-0353518. The authors are deeply grateful for the help received in the course of this investigation from Curtis D. Clayton, Propulsion Lead, Missile Defense Target Vehicles, Lockheed Martin Space Systems Company.

References

[1] Sutton, G. P., *Rocket Propulsion Elements*, 6th ed., John Wiley, New York, 1992.

[2] Coats, D. E., and Dunn, S. S., "*Solid Performance Program (SPP) Version 7.2 VAV*," Software and Engineering Associates, Inc., Report No. SEA TR 95-021995.

[3] Nickerson, G. R., Coats, D. E., Hersmen, R. L., and Lamberty, J., "A Computer Program for the Prediction of Solid Propellant Rocket Motor Performance (SPP)," Software and Engineering Associates, Inc., AFRPL TR-83-036, CA, Sept. 1983.

[4] Coats, D. E., and Dunn, S. S., "Improved Motor Stability Predictions for 3D Grains Using the SPP Code," AIAA Paper 97-33251, July 1997.

[5] Sabnis, J. S., Gibeling, H. J., and McDonald, H., "Navier–Stokes Analysis of Solid Propellant Rocket Motor Internal Flows," *Journal of Propulsion and Power*, Vol. 5, No. 6, 1989, pp. 657–664.

[6] Fiedler, R. A., Jiao, X., Namazifard, A., Haselbacher, A., Najjar, F. M., and Parsons, I. D., "Coupled Fluid-Structure 3-D Solid Rocket Motor Simulations," AIAA Paper 2001-3954, July 2001.

[7] Venugopal, P., Najjar, F. M., and Moser, R. D., "DNS and LES Computations of Model Solid Rocket Motors," AIAA Paper 2000-3571, July 2000.

[8] Venugopal, P., Najjar, F. M., and Moser, R. D., "Numerical Simulations of Model Solid Rocket Motor Flows," AIAA Paper 2001-3950, July 2001.

[9] Wasistho, B., Haselbacher, A., Najjar, F. M., Tafti, D., Balachandar, S., and Moser, R. D., "Direct and Large Eddy Simulations of Compressible Wall-Injection Flows in Laminar, Transitional, and Turbulent Regimes," AIAA Paper 2002-4344, July 2002.

[10] Culick, F. E. C., "Rotational Axisymmetric Mean Flow and Damping of Acoustic Waves in a Solid Propellant Rocket," *AIAA Journal*, Vol. 4, No. 8, 1966, pp. 1462–1464.

[11] Zhou, C., and Majdalani, J., "Improved Mean Flow Solution for Slab Rocket Motors with Regressing Walls," *Journal of Propulsion and Power*, Vol. 18, No. 3, 2002, pp. 703–711.

[12] Majdalani, J., Vyas, A. B., and Flandro, G. A., "Higher Mean-Flow Approximation for a Solid Rocket Motor with Radially Regressing Walls," *AIAA Journal*, Vol. 40, No. 9, 2002, pp. 1780–1788.

[13] Majdalani, J., "The Compressible Taylor–Culick Flow," AIAA Paper 2005-3542, July 2005.

[14] Majdalani, J., and Vyas, A. B., "Inviscid Models of the Classic Hybrid Rocket," AIAA Paper 2004-3474, July 2004.

[15] Majdalani, J., "The Taylor-Culick Profile with Uniform Headwall Injection," AIAA Paper 2005-4534, July 2005.

[16] Majdalani, J., and Flandro, G. A., "The Oscillatory Pipe Flow with Arbitrary Wall Injection," *Proceedings of the Royal Society of London, Series A: Mathematical and Physical Sciences*, Vol. 458, No. 2022, 2002, pp. 1621–1651.

[17] Majdalani, J., and Roh, T. S., "The Oscillatory Channel Flow with Large Wall Injection," *Proceedings of the Royal Society of London, Series A: Mathematical and Physical Sciences*, Vol. 456, No. 1999, 2000, pp. 1625–1657.

[18] Majdalani, J., "The Oscillatory Channel Flow with Arbitrary Wall Injection," *Journal of Applied Mathematics and Physics*, Vol. 52, No. 1, 2001, pp. 33–61.

[19] Majdalani, J., and Van Moorhem, W. K., "*Improved Time-Dependent Flowfield Solution for Solid Rocket Motors*," *AIAA Journal*, Vol. 36, No. 2, 1998, pp. 241–248.

[20] Majdalani, J., "The Boundary Layer Structure in Cylindrical Rocket Motors," *AIAA Journal*, Vol. 37, No. 4, 1999, pp. 505–508.

[21] Majdalani, J., Flandro, G. A., and Roh, T. S., "Convergence of Two Flowfield Models Predicting a Destabilizing Agent in Rocket Combustion," *Journal of Propulsion and Power*, Vol. 16, No. 3, 2000, pp. 492–497.

[22] Majdalani, J., Flandro, G. A., and Fischbach, S. R., "Some Rotational Corrections to the Acoustic Energy Equation in Injection-Driven Enclosures," *Physics of Fluids*, Vol. 17, No. 7, 2005, pp. 07410201–20.

[23] Malhotra, S., and Flandro, G. A., "On the Origin of the DC Shift," AIAA Paper 97-3249, July 1997.

[24] Flandro, G. A., Fischbach, S. R., Majdalani, J., and French, J. C., "Nonlinear Rocket Motor Stability Prediction: Limit Amplitude, Triggering, and Mean Pressure Shift," AIAA Paper 2004-4054, July 2004.

[25] Flandro, G. A., Majdalani, J., and Sims, J. D., "Nonlinear Longitudinal Mode Instability in Liquid Propellant Rocket Engine Preburners," AIAA Paper 2004-4162, July 2004.

[26] Féraille, T., and Casalis, G., "Channel Flow Induced by Wall Injection of Fluid and Particles," *Physics of Fluids*, Vol. 15, No. 2, 2003, pp. 348–360.

[27] Thomas, H. D., Flandro, G. A., and Flanagan, S. N., "Effects of Vorticity on Particle Damping," AIAA Paper 95-2736, July 1995.

[28] Rao, N. X., and Van Moorhem, W. K., "Interactions of Particles with the Flow near the Burning Surface of a Solid Propellant Rocket," AIAA Paper 93-0110, Jan. 1993.

[29] Elgobashi, S., "On Predicting Particle-Laden Turbulent Flows," *Applied Scientific Research*, Vol. 52, No. 4, June 1994, p. 309.

[30] Sabnis, J. S., de Jong, F. J., and Gibeling, H. J., "Calculation of Particle Trajectories in Solid-Rocket Motors with Arbitrary Acceleration," *Journal of Propulsion and Power*, Vol. 8, No. 5, 1992, pp. 961–967.

[31] Vuillot, F., Dupays, J., Lupoglazoff, N., Basset, T., and Daniel, E., "2-D Navier–Stokes Stability Computations for Solid Rocket Motors: Rotational, Combustion and Two-Phase Flow Effects," AIAA Paper 97-3326, July 1997.

[32] Lupoglazoff, N., and Vuillot, F., "Parietal Vortex Shedding as a Cause of Instability for Long Solid Propellant Motors. Numerical Simulations and Comparisons with Firing Tests," AIAA Paper 96-0761, Jan. 1996.

[33] Lupoglazoff, N., and Vuillot, F., "Numerical Simulations of Parietal Vortex-Shedding Phenomenon in a Cold-Flow Set-Up," AIAA Paper 98-3220, July 1998.

[34] Couton, D., Doan-Kim, S., and Vuillot, F., "Numerical Simulation of Vortex-Shedding Phenomenon in a Channel with Flow Induced through Porous Wall," *International Journal of Heat and Fluid Flow*, Vol. 18, No. 3, 1997, pp. 283–296.

[35] Griffond, J., Casalis, G., and Pineau, J.-P., "Spatial Instability of Flow in a Semiinfinite Cylinder with Fluid Injection through Its Porous Walls," *European Journal of Mechanics, B/Fluids*, Vol. 19, No. 1, 2000, pp. 69–87.

[36] Casalis, G., Avalon, G., and Pineau, J.-P., "Spatial Instability of Planar Channel Flow with Fluid Injection through Porous Walls," *Physics of Fluids*, Vol. 10, No. 10, 1998, pp. 2558–2568.

[37] Griffond, J., and Casalis, G., "On the Nonparallel Stability of the Injection Induced Two-Dimensional Taylor Flow," *Physics of Fluids*, Vol. 13, No. 6, 2001, pp. 1635–1644.

[38] Griffond, J., and Casalis, G., "On the Dependence on the Formulation of Some Nonparallel Stability Approaches Applied to the Taylor Flow," *Physics of Fluids*, Vol. 12, No. 2, 2000, pp. 466–468.

[39] French, J. C., Flandro, G. A., and Majdalani, J., "Improvements to the Linear Standard Stability Prediction Program (SSP)," AIAA Paper 2004-4181, July 2004.

[40] Clayton, C. D., "Flowfields in Solid Rocket Motors with Tapered Bores," AIAA Paper 96-2643, July 1996.

[41] Anon., *Fluent UNS Theory Manual*, 6.1 ed., Fluent Inc., Palo Alto, California, 2002.

[42] Brown, R. S., Blackner, A. M., Willoughby, P. G., and Dunlap, R.,

"Coupling between Acoustic Velocity Oscillations and Solid Propellant Combustion," *Journal of Propulsion and Power*, Vol. 2, No. 5, 1986, pp. 428–437.

[43] Dunlap, R., Blackner, A. M., Waugh, R. C., Brown, R. S., and Willoughby, P. G., "Internal Flow Field Studies in a Simulated Cylindrical Port Rocket Chamber," *Journal of Propulsion and Power*, Vol. 6, No. 6, 1990, pp. 690–704.

[44] Apte, S., and Yang, V., "Effect of Acoustic Oscillation on Flow Development in a Simulated Nozzleless Rocket Motor," *Solid Propellant Chemistry, Combustion, and Motor Interior Ballistics*, Vol. 185, edited by V. Yang, T. B. Brill, and W.-Z. Ren, AIAA Progress in Astronautics and Aeronautics, Washington, DC, 2000, pp. 791–822.

J. Oefelein
Associate Editor